

## Chapter 9

# Insect-Inspired Odometry by Optic Flow Recorded with Optical Mouse Chips

Hansjürgen Dahmen, Alain Millers, and Hanspeter A. Mallot

**Abstract** Inspired by investigations in water striders (*Gerrids*) on the eye structure and visually controlled behaviour and subsequent simulations of self-motion estimates from optic flow, a device is presented that extracts self-motion parameters exclusively from flow. Optical mouse chips provided with adequate lenses serve as motion sensors. Pairs of sensors with opposite lines of sight are mounted on a sensor head. The optical axes of the sensor pairs are distributed over the largest possible solid angle. The device is fast, cheap and light. The calibration procedure and tests on the precision of self-motion estimates in outdoor experiments are reported.

### 9.1 Introduction

Optic flow (OF) is used in many insects for flight control [27]. Bees control landing, flight speed and travelling distance by OF [1, 24, 23, 25]. There is a vast literature on the influence of OF in various species of flies on the control of flight speed, chasing behaviour and turning responses [8, 9, 13, 10]. The present work was inspired by findings on the visually controlled behaviour of water striders (*Gerris lacustris*, *Gerris paludum*). Water striders compensate precisely for self-rotation and self-translation by separate responses [16, 17]. Their eye is divided into three morphologically and functionally distinguished zones, a dorsal, horizontal and ventral one [5]. The

self-rotation response is limited to the dorsal part which comprises about 30% of the ca. 800 ommatidia of one eye. In the dorsal eye we find relatively large interommatidial angles of more than  $10^\circ$ . The good self-rotation compensation led us to investigate precision limits for the estimation of self-motion parameters from OF in a static surround under various environmental conditions using different parts of the visual field [6, 7]. In these studies the algorithm proposed by Koenderink and van Doorn [18] for spherical wide-field eyes was used. The result was that self-motion can be extracted from flow to a surprisingly high precision if flow can be observed by detector pairs which look along opposite lines of sight and if these pairs are distributed over a large solid angle. Under these conditions only a few properly combined flow observations are necessary. The extraction of self-motion from flow by matched filters inspired by observations on wide-field neurons in flies has been investigated by Franz and Krapp [12].

Besides the interest in the exploitation of OF in animals there is a lot of work in robotics devoted to reveal the structure of the environment from flow induced by self-motion and/or to determine and control self-motion by OF [28, 11]. To extract self-motion from flow Baker and Pless proved that omnidirectional view helps a lot to eliminate ambiguities in the evaluation of self-rotation and -translation [2, 21]. There have been developed various catadioptric systems to realize omnidirectional vision with a single camera [4, 19, 15]. The approach most similar to ours is the so-called argus eye [2, 3]. In this system several cameras with non overlapping visual fields looking into opposite directions cooperate to reveal self-motion parameters and structure of the environment. Besides the difficulty to calibrate such a system, one has to deal

---

H. Dahmen (✉)  
Cognitive Neurosciences, University of Tübingen, Germany  
e-mail: hansjuergen.dahmen@uni-tuebingen.de

with the integration of the output of several cameras [21]. We wanted to test a much simpler and faster setup monitoring flow by commercially available dedicated flow detectors.

With the development of optical mouse chips cheap (2.5 Euro), light (0.5 g) and fast (response time < 1 ms) flow detectors have become available. Here we present a hardware realization of an odometer driven solely by flow measurements along a few lines of sight in space.

## 9.2 Hardware Implementations

Two prototypes of sensor heads have been constructed so far. Head A (Fig. 9.1) is designed for ground moving robots for which the distance to the ground does not change much. These vehicles are supposed to have for self-motion only 2 degrees of freedom (DOF), yaw and

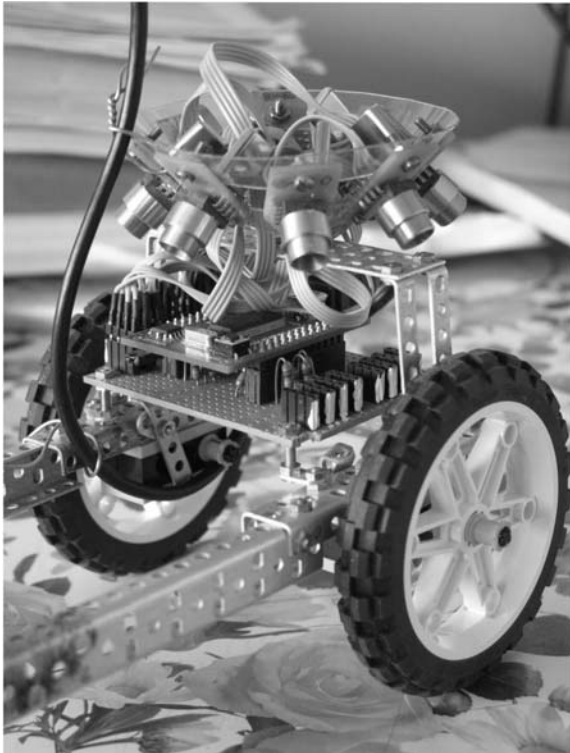


**Fig. 9.1** Head A contains eight optical mouse sensors (ADNS2620, Avago) looking down to the ground at about  $-45^\circ$  relative to the horizon. Each sensor is equipped with an adjustable plastic collimator lens (CAY046 Philips) of  $f = 4.6$  mm focal length which images the floor onto the light-sensitive area of the sensor

translation along their long axis. Head B (Fig. 9.2) is intended to extract all the possible information about self-motion that can be obtained from optical flow: 3 DOF of rotation, (as is well known, see Sect. 9.4) only the direction of translation (2 DOF) but not its absolute size, and the ‘relative nearness’ of the environment seen by each sensor.

The mouse sensors ADNS2620 sample the light intensity on their  $1 \times 1$  mm array of  $18 \times 18$  light-sensitive diodes about 1500 times/s. The focal length of the lens ( $f = 4.6$  mm) and the size of the diode array determine the angular size of the visual field of the sensors to  $12.4^\circ \times 12.4^\circ$ . A fast on-chip digital signal processor (DSP) correlates the patterns of two consecutive samplings and evaluates the displacement between them. In order to avoid too large displacements between two images the maximum allowed speed of the pattern on the chip’s light-sensitive surface is limited to 30 cm/s. This limits the maximum rotation speed of the sensors to  $(300 \times 180/\pi)/f$  [ $^\circ/\text{s}$ ] (i.e. 3737 [ $^\circ/\text{s}$ ]). When the viewing distance to ground is  $D$  [cm] the maximum translational speed is  $(300/f)D = 65.22 D$  [cm/s] (i.e. about 980 [cm/s] for  $D = 15$  cm). The minimal displacement detectable on the sensor surface is 1/16 mm. With the focal length of 4.6 mm this leads to an angular resolution of  $0.778^\circ$  and at the distance of 15 cm to a minimal detectable displacement of 2.04 mm.

A microprocessor ( $\mu\text{P}$ ) (CY7C68013A-56P, Cypress) reads information continuously from all sensors in parallel and synchronously (Fig. 9.3). The information consists of three bytes:  $dY$ ,  $dX$ , SQ in that order.  $dY$ ,  $dX$  are the pattern displacements along each sensor’s  $Y/X$ -axis since the last reading; SQ is a ‘quality’ byte which indicates the ‘number of features’ detected in the sensor image while correlating. If SQ undergoes a selectable threshold  $dY$ ,  $dX$  may be unreliable and discarded. Reading the information from all sensors (strictly in parallel) and transferring them via an USB1.1 bulk transfer to the PC costs less than 2 ms.

## 9.3 Calibration

In order to use these heads for odometry, the line of sight, the  $X/Y$ -orientation relative to the head coordinate system and the sensitivity of each sensor have to

**Fig. 9.2** Head B contains two sets of eight sensors each, one above the other below the aluminium plate in (a). The eight sensors of the upper set look under about 45° of azimuth with respect to each other into the horizon, only four can be seen in (b). The lower set looks down to the ground in a similar way as in head A (c). The eight horizontally looking sensors are equipped with the same but non adjustable lenses as the down looking sensors

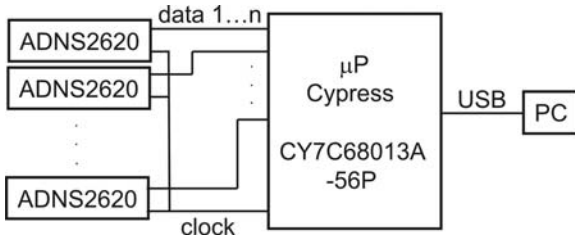
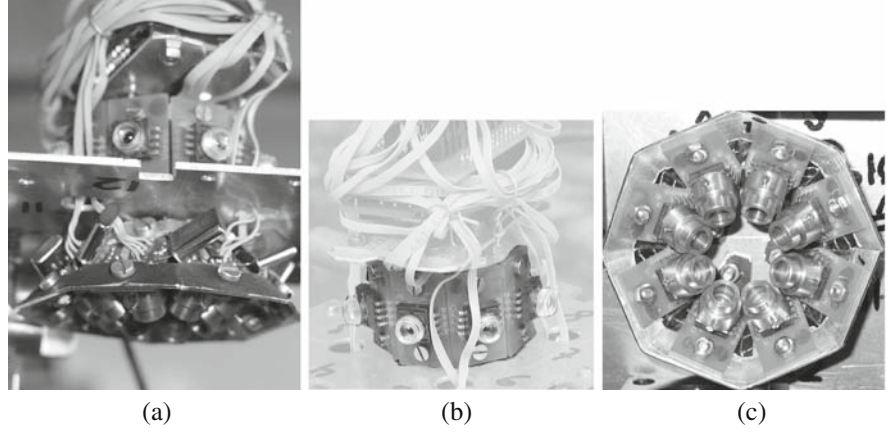


**Fig. 9.3** Circuit diagram of the odometer. A microprocessor ( $\mu$ P) (CY7C68013A-56P, Cypress) reads information continuously from all sensors in parallel via two serial lines to each sensor: a clock- and a data line. The clock line is common to all sensors, the data line of each sensor is connected to an individual I/O pin on the  $\mu$ P. The  $\mu$ P is connected to a PC via USB

be determined. In order to reveal these parameters the heads have to undergo a calibration procedure.

### 9.3.1 Head A

For the eight-sensor head A the task is very simple: The head is moved along a defined straight line or rotated around a defined angle and the output of all sensors is registered (Fig. 9.4). From these responses we get for each sensor  $i$  ‘unit’ responses  $\mathbf{a}^i = (a_x^i, a_y^i)^\top$  ( $^\top$  means transposed) to 1 cm translation and  $\mathbf{b}^i = (b_x^i, b_y^i)^\top$  to 1° of rotation. The response  $\mathbf{c}^i = (c_x^i, c_y^i)^\top$  to a combined motion of  $\tau$  cm of translation and  $\rho$  degrees of yaw is given by

$$\mathbf{c}^i = \tau \mathbf{a}^i + \rho \mathbf{b}^i \quad (9.1)$$

### 9.3.2 Head B

In order to determine the orientation and sensitivity of each sensor in the coordinate system of head B, the following calibration procedure was proposed by A. Schilling (personal communication). We rotate head B about its  $X$ -,  $Y$ -,  $Z$ -axis by defined angles and read the sensors’ output. Let  $(X, Y, Z)^\top$  be the sensor head coordinate system, and  $(X_s^i, Y_s^i, Z_s^i)^\top$  the  $i$ th sensor coordinate system with  $Z_s^i$  pointing along the line of sight. Let the rotation matrix  $R^i$  describe the rotation of  $(X, Y, Z)^\top$  into  $(X_s^i, Y_s^i, Z_s^i)^\top$

$$\begin{pmatrix} X_s^i \\ Y_s^i \\ Z_s^i \end{pmatrix} = R^i \begin{pmatrix} X \\ Y \\ Z \end{pmatrix}; \quad R^i = \begin{pmatrix} r_{11}^i & r_{12}^i & r_{13}^i \\ r_{21}^i & r_{22}^i & r_{23}^i \\ r_{31}^i & r_{32}^i & r_{33}^i \end{pmatrix} \quad (9.2)$$

A rotation  $\omega_s^i = (\omega_{xs}^i, \omega_{ys}^i, \omega_{zs}^i)^\top$  in the  $i$ th sensor’s coordinate system leads to a sensor response  $\mathbf{c}^i$  (there is no response to  $\omega_{zs}^i$ ):

$$\mathbf{c}^i = \begin{pmatrix} c_x^i \\ c_y^i \end{pmatrix} = f^i \begin{pmatrix} -\omega_{ys}^i \\ \omega_{xs}^i \end{pmatrix} = f^i \begin{pmatrix} 0 & -1 & 0 \\ 1 & 0 & 0 \end{pmatrix} R^i \omega \quad (9.3)$$

$f^i$  reflects the ‘sensitivity’ of the sensor  $i$  (proportional to the focal length of its lens). The rotation in the

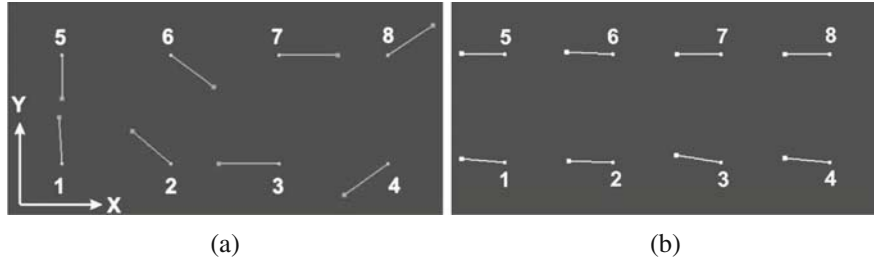


**Fig. 9.4** The  $X/Y$ -response of the eight sensors of head A to (a) 15 cm of straight translation and (b) a pure  $45^\circ$  counterclockwise rotation. The smaller points ( $\circ$ ) near the sensor numbers mark the sensor response at the start and the larger points ( $\diamond$ ) at

the end of the movement. From responses to larger translations and rotations we extract for each sensor  $i$  'unit' responses  $\mathbf{a}^i$  to 1 cm of translation and  $\mathbf{b}^i$  to  $1^\circ$  of rotation

sensor coordinate system is given by  $\omega_s^i = \mathbf{R}^i \omega$ , with  $\omega$  being the rotation in the head coordinate system.

Choosing  $\omega$  along the  $X$ -,  $Y$ -,  $Z$ -axis, respectively, with the rotation angle  $\|\omega\| = \phi$  reveals the first two rows of  $\mathbf{R}^i$ . In Sect. 9.4 it will be shown that  $f^i$  and the third row of  $\mathbf{R}^i$  are not needed for odometry.

$$\omega = \phi \begin{pmatrix} 1 \\ 0 \\ 0 \end{pmatrix} \Rightarrow \mathbf{c}^i = \phi \begin{pmatrix} -r_{21}^i \\ r_{11}^i \end{pmatrix}$$

$$\omega = \phi \begin{pmatrix} 0 \\ 1 \\ 0 \end{pmatrix} \Rightarrow \mathbf{c}^i = \phi \begin{pmatrix} -r_{22}^i \\ r_{12}^i \end{pmatrix}$$

$$\omega = \phi \begin{pmatrix} 0 \\ 0 \\ 1 \end{pmatrix} \Rightarrow \mathbf{c}^i = \phi \begin{pmatrix} -r_{23}^i \\ r_{13}^i \end{pmatrix}$$

To calibrate head B, it was mounted on a Spindler & Hoyer micro-optical bench. The bench was then fixed on a cylinder which could be rotated by precisely controlled angles by a stepper motor (1067 steps /  $360^\circ$ ) about the vertical axis (Fig. 9.5). The head's  $X$ -,  $Y$ - and  $Z$ -axis could be precisely oriented along the rotation axis. The head was surrounded by a contrasted environment. In particular head orientations some of the sensors were always blocked by the bench to see the contrasted environment, but there were always other

head orientations which allowed to monitor the sensor responses to head rotation and thus calibrate the response of each sensor. Calibration means to determine the matrix elements of  $\mathbf{R}^i$ . The  $X/Y$ -response of all sensors (except the blocked ones) versus step count is a straight line, the slope of which reflects the sensitivity of each sensor to the actual rotation. Figure 9.5c,d shows as an example the  $X/Y$ -response for the calibration about the  $Z$ -axis. The inset shows the enlarged response. Because of the  $X/Y$ -orientation of the sensors, rotation around the  $Z$ -axis leads only to a very small  $Y$ -response (Fig. 9.5d, note the scale). The inset of Fig. 9.5c and Fig. 9.5d demonstrate the monotonic response of the sensors to small monotonic motion. Note the motor step size of  $0.337^\circ$  in comparison to the minimum detectable angular displacement of a single sensor of about  $0.778^\circ$  (see Sect. 9.2). There is no additional noise visible.

We obtain  $(r_{23}^i, r_{13}^i)^\top$  from the slope in Fig. 9.5c,d. In a similar way we evaluate  $(r_{21}^i, r_{11}^i)^\top$  from responses to rotation about the head's  $X$ -axis and  $(r_{22}^i, r_{12}^i)^\top$  from rotation about the  $Y$ -axis.

## 9.4 Odometry

Self-motion can be decomposed at each moment uniquely into a self-rotation  $\omega$  and a self-translation  $\mathbf{T}$ .

From flow alone one can only hope to retrieve self-rotation  $\omega$  (3 DOF), the direction of self-translation  $\mathbf{t}$  (2 DOF) and  $T / d^i$  the ratio of speed over distance to contrast in the line of sight of each sensor, the so-called 'relative nearness' [18].

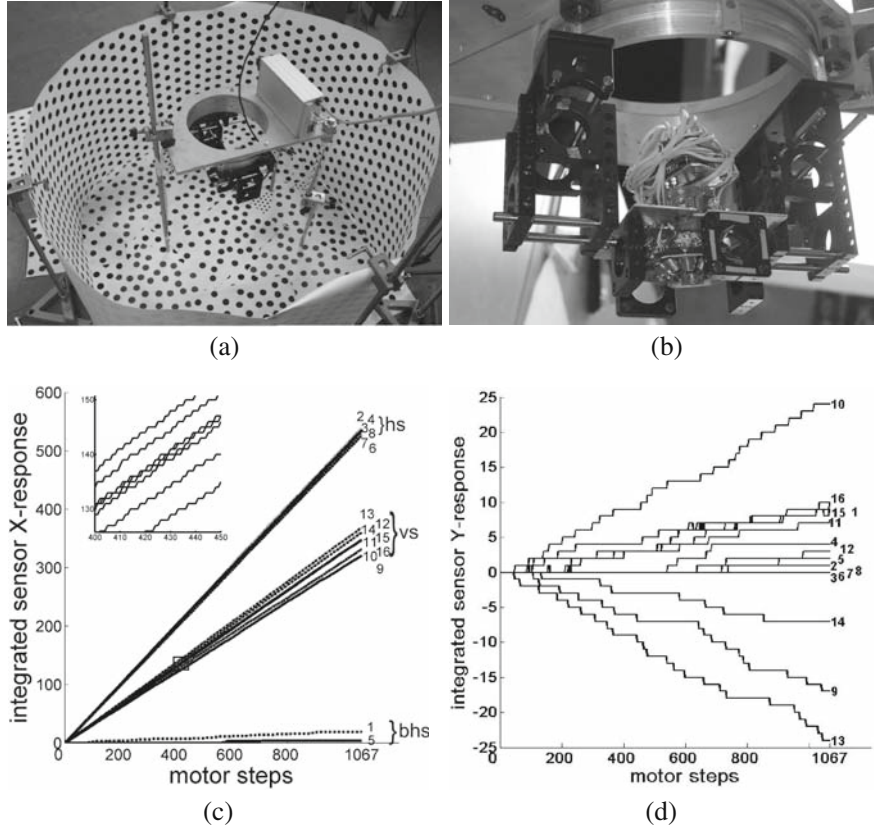


**Fig. 9.5** Head B was mounted on a Spindler & Hoyer micro-optical bench (b). The bench was mounted on a cylinder which could be rotated about the vertical axis in a contrasted environment by a stepper motor (1067 steps/360°) (a). The head's X-, Y- and Z-axis could be precisely oriented along the rotation axis. The X-response of the 16 sensors to ccw rotation about the head's Z-axis is shown in (c). Some of the sensors were visually blocked by the optical bench in this special head orientation (bhs), hs

indicates the X-responses of the horizontally oriented sensors, vs the response of the sensors oriented downwards. The inset shows the enlarged response. Because of the sensor orientation, rotation around the Z-axis leads only to a very small Y-response (d) (note the scale). The sensor responses in (d) as well as in the inset in (c) demonstrate the monotonic response of the sensors to small monotonic motion. For further explanation see text

#### 9.4.1 Head A

In the case of only 2 DOF the parameters  $\tau$  of translation along the X-axis  $\mathbf{T} = (\tau, 0, 0)^\top$  and  $\rho$  of yaw  $\omega = (0, 0, \rho)^\top$  can easily be extracted: minimizing  $E$ , the sum of squared deviations

$$E = \sum_i (\mathbf{c}^i - \tau \mathbf{a}^i - \rho \mathbf{b}^i)^2 \quad (9.4)$$

( $\mathbf{c}^i$  = sensor response,  $\mathbf{a}^i$  = 'unit' response to 1 cm translation,  $\mathbf{b}^i$  = 'unit' response to 1° of yaw) leads to the best linear fit for  $\tau, \rho$ :

$$\tau = \left( \sum_i \mathbf{a}^i \mathbf{c}^i \sum_i \mathbf{b}^{i2} - \sum_i \mathbf{a}^i \mathbf{b}^i \sum_i \mathbf{b}^i \mathbf{c}^i \right) / \gamma \quad (9.5)$$

$$\rho = \left( \sum_i \mathbf{a}^{i2} \sum_i \mathbf{b}^i \mathbf{c}^i - \sum_i \mathbf{a}^i \mathbf{c}^i \sum_i \mathbf{a}^i \mathbf{b}^i \right) / \gamma \quad (9.6)$$

with

$$\gamma = \sum_i \mathbf{a}^{i2} \mathbf{b}^{i2} - \left( \sum_i \mathbf{a}^i \mathbf{b}^i \right)^2 \quad (9.7)$$

### 9.4.2 Head B

The response  $\mathbf{c}^i$  of sensor  $i$  to self-motion of combined translation  $\mathbf{T} = (T_x, T_y, T_z)^\top$  and rotation  $\omega = (\omega_x, \omega_y, \omega_z)^\top$  is given by

$$\mathbf{c}^i = \begin{pmatrix} c_x^i \\ c_y^i \end{pmatrix} = \begin{pmatrix} 0 & -1 & 0 \\ 1 & 0 & 0 \end{pmatrix} \mathbf{R}^i \omega + f^i \frac{1}{d^i} \begin{pmatrix} 1 & 0 & 0 \\ 0 & 1 & 0 \end{pmatrix} \mathbf{R}^{i\top} \quad (9.8)$$

With

$$\mathbf{A}^i = f^i \begin{pmatrix} 1 & 0 & 0 \\ 0 & 1 & 0 \end{pmatrix} \mathbf{R}^i = f^i \begin{pmatrix} r_{11}^i & r_{12}^i & r_{13}^i \\ r_{21}^i & r_{22}^i & r_{23}^i \end{pmatrix} \quad (9.9)$$

and

$$\mathbf{B}^i = f^i \begin{pmatrix} 0 & -1 & 0 \\ 1 & 0 & 0 \end{pmatrix} \mathbf{R}^i = f^i \begin{pmatrix} -r_{21}^i & -r_{22}^i & -r_{23}^i \\ r_{11}^i & r_{12}^i & r_{13}^i \end{pmatrix} \quad (9.10)$$

$\mathbf{c}^i$  can be rewritten as

$$\mathbf{c}^i = \mathbf{B}^i \omega + \frac{1}{d^i} \mathbf{A}^i \mathbf{T} \quad (9.11)$$

Minimizing  $E = \sum_i (\mathbf{c}^i - \hat{\mathbf{c}}^i)^2$  ( $\hat{\mathbf{c}}^i$  = measured responses) leads to ‘best-fit’ estimates for  $\omega$ ,  $\mathbf{T}$ ,  $1/d^i$ :

$$\omega = \Lambda \sum_i \mathbf{B}^{i\top} \left( \hat{\mathbf{c}}^i - \frac{1}{d^i} \mathbf{A}^i \mathbf{T} \right) \text{ with } \Lambda = \left( \sum_i \mathbf{A}^i \mathbf{A}^{i\top} \right)^{-1} \quad (9.12)$$

$$\mathbf{T} = K \sum_i \frac{1}{d^i} \mathbf{A}^{i\top} \left( \hat{\mathbf{c}}^i - \mathbf{B}^i \omega \right) \text{ with } K = \left( \sum_i \frac{1}{d^{i2}} \mathbf{A}^i \mathbf{A}^{i\top} \right)^{-1} \quad (9.13)$$

$$\frac{1}{d^i} = P^i \mathbf{T}^\top \mathbf{A}^{i\top} \left( \hat{\mathbf{c}}^i - \mathbf{B}^i \omega \right) \text{ with } P^i = \left( \mathbf{T}^\top \mathbf{A}^i \mathbf{A}^{i\top} \mathbf{T} \right)^{-1} \quad (9.14)$$

### 9.4.3 Fast Estimates

The equations for best-fit  $\omega$ ,  $\mathbf{T}$ ,  $1/d^i$  can only be solved by an iterative procedure. However, we found that

often a simplified estimate comes close to the best fit. For the rotation  $\omega$  a good fit is

$$\omega = \Lambda \sum_i \mathbf{B}^{i\top} \hat{\mathbf{c}}^i \quad (9.15)$$

summed over the eight horizontal sensors only and omitting the correction term containing  $\mathbf{T}$ , the so-called ‘apparent rotation’ induced by the translation. This simplification works well in environments where the distance to objects seen by the horizontally oriented sensors are large enough to induce only a small flow component by  $\mathbf{T}$  compared to that induced by  $\omega$ . In addition the horizontal sensors are paired which reduces the error in  $\omega$  induced by  $\mathbf{T}$ . In this context it is of interest that water striders also limit their response to self-rotation to the dorsal eye. For the translation the estimate

$$\mathbf{T} = \Lambda \sum_i \mathbf{A}^{i\top} (\hat{\mathbf{c}}^i - \mathbf{B}^i \omega) \quad (9.16)$$

omitting the individual factor  $1/d^i$  for each sensor (assuming  $d^i$  to be constant) produces acceptable estimates for  $\mathbf{T}$  in environments with a not too inhomogeneous distance distribution. With the above estimates of  $\omega$ ,  $\mathbf{T}$  an estimate for  $1/d^i$  is

$$\frac{1}{d^i} = P^i \mathbf{T}^\top \mathbf{A}^{i\top} (\hat{\mathbf{c}}^i - \mathbf{B}^i \omega) \quad (9.17)$$

$\|\mathbf{T}\|/d^i$  is the ‘relative nearness’.

## 9.5 Tests

In order to test the performance of both heads we carried out several experiments. It turned out that especially for head B in an outdoor environment good results can be obtained by the fast estimates of self-motion. Outdoor we find usually rich contrast around the horizon and acceptable distributions of ‘relative nearnesses’ around the sensor head.

### 9.5.1 Head A

In order to get an estimate for the precision of odometer results for the eight-sensor head A it was moved manually 20 times along a straight line for distances  $\tau$  of 20, 40, 60 and 80 cm and rotated 20 times around the vertical axis by  $\rho = 90^\circ, 180^\circ, 270^\circ$  and  $360^\circ$ . We cannot give an error estimate for the hand guidance error. Rotating the currcle on the spot without introducing an X- and/or Y-displacement turned out to be somewhat delicate. Averages and standard deviations of estimates  $\bar{\tau}$  and  $\bar{\rho}$  for these trials are given in Table 9.1.

**Table 9.1** Test results for head A

$\tau$ [cm]	avg $\bar{\tau}$ [cm]	std( $\bar{\tau}$ ) [cm]
translation		
20	19.8495	0.1072
40	39.875	0.1064
60	59.8995	0.1425
80	79.9285	0.1710
rotation		
$\rho$ [deg]	avg $\bar{\rho}$ [deg]	std( $\bar{\rho}$ ) [deg]
90	90.0205	0.4356
180	180.3925	0.6167
270	271.1805	0.5264
360	360.664	0.8132

### 9.5.2 Head B

#### 9.5.2.1 Test for the Orientation and Size of the Estimated Rotation

For the 16-sensor head B first we wanted to find out the quality of pure rotation results about various axis

orientations. Head B was rotated clock- and counter-clockwise on the optical bench by a fixed angle  $\rho$ . The orientation  $\alpha$  of the axis of rotation  $\omega$  was varied in the X/Z plane of the head (Fig. 9.6b).

The results of fast estimates are indicated in Fig. 9.6a. Deviations between the expected  $\omega$  and the estimated one are mainly due to errors in the alignment by hand of the  $\omega$ -axis as can be seen from the errors for

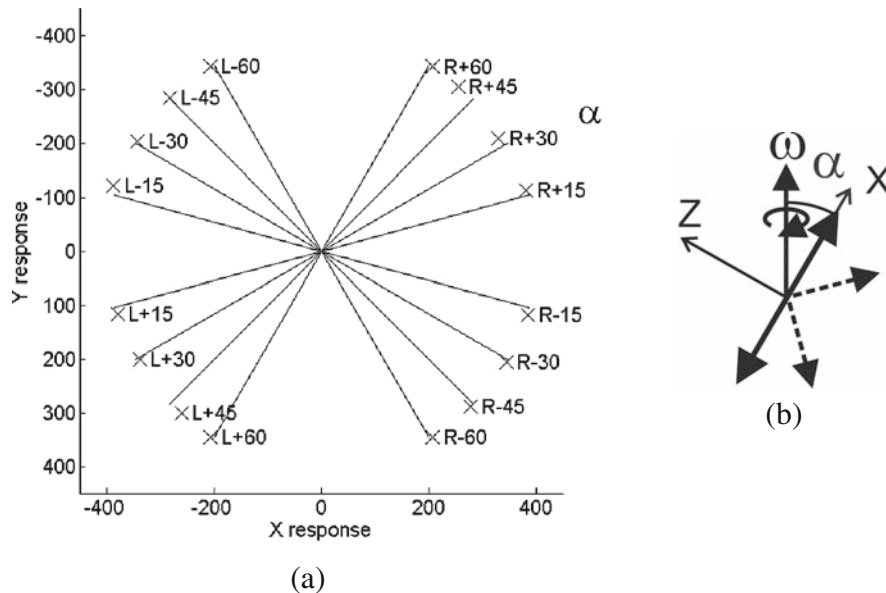


**Fig. 9.6** Head B was rotated cw and ccw on the optical bench by a fixed angle  $\rho$  about the rotation axis  $\omega$ . The orientation  $\alpha$  of the rotation axis was varied in the X/Z plane of the head. In Fig. 9.6b the thick arrows indicate the line of sight of the horizontal sensors of head B, the dashed ones that of the sensors looking downwards.  $\omega$  illustrates the rotation axis. The inclination  $\alpha$  of  $\omega$  was adjusted by hand using a plastic set square. In

Fig. 9.6a the tips of the ‘fast estimated’ vector  $\omega$  are indicated as crosses. The lines represent expected rotation vectors if the adjustment by hand would have been correct. R, L indicate ccw and cw rotation, respectively; the numbers indicate  $\alpha$ . For a discussion of deviations between expected and estimated  $\omega$  see text



opposite  $\omega$ -axes (e.g. for L+45 and R+45). For opposite  $\omega$ -axes the mechanical adjustment and therefore the misalignment of the rotation axis was the same. So the deviation from the expected orientation should be the same. We conclude that the orientation of the  $\omega$ -axis is well represented by the estimated one. Also the size  $\rho$  of the rotation (reflected by the length of the lines) is well represented by the ‘fast estimates’ of  $\omega$  (the distance of the crosses from the origin). We conclude from this test that (in the case of zero translation) all coordinates of  $\omega$  are satisfactorily reproduced by the fast estimate calculus of  $\omega$ .

### 9.5.2.2 Outdoor Test of T- and $\omega$ -Distribution

Next we wanted to find out the quality of  $\omega$  and  $T$  results for a superimposed rotation and translation in an outdoor environment with more or less constant ‘relative nearnesses’. An outdoor environment under daylight is highly appropriate for the sensors because sufficient contrast with a broad spectrum of spatial frequencies is visible.

Head B was mounted on a rod (Fig. 9.7a) in an outdoor environment and moved by a stepper motor with constant angular velocity along a horizontal circle of 75 cm radius at a height of 40, 61.5 and 90 cm above the ground ( $1067 \text{ steps} \equiv 360^\circ$ ). Figure 9.7a shows the hardware setup, Fig. 9.7b depicts the X-response of the 16 sensors for the case of 61.5 cm height of the circle. The orientation of the sensors (seen from above) is indicated in Fig. 9.7c. In order to test the distribution of fast  $\omega$ - and  $T$ -estimates 38 subsets of 50 successive motor steps (i.e. of  $16.82^\circ$  rotation angle of the rod) were selected along the whole circular head path. For these subsets we expect  $\omega$  to be oriented along the Z-axis:  $\omega = (0, 0, 16.82^\circ)^\top$  and  $T$  to be oriented along the X-axis:  $T = (T_x, 0, 0)^\top$ .  $T_x$  can roughly be estimated as  $8.44^\circ$  (Fig. 9.8).

Figure 9.9 shows the distribution, the mean and standard deviation of  $\omega_x$ ,  $\omega_y$ ,  $\omega_z$  and  $T_x$ ,  $T_y$ ,  $T_z$  for the 38 subsets. The mean of the various components deviates from the expected values by less than  $1^\circ$ .

To test if our ‘fast estimates’ are near to a minimum of  $E$ , a Levenberg–Markwardt iteration (LMI) [22]

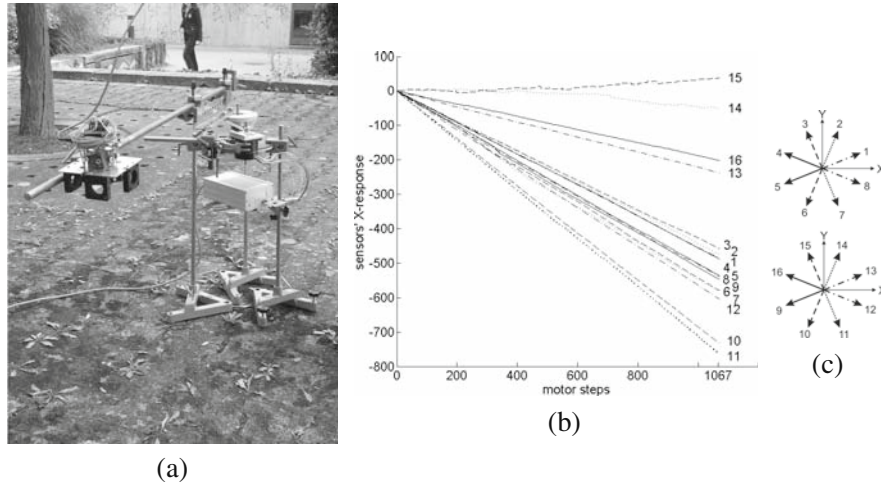


**Fig. 9.7** Head B was mounted on a rod (Fig. 9.7a) and moved by a stepper motor with constant angular velocity along a horizontal circle of 75 cm radius at a height of 61.5 cm above the ground in an outdoor environment. The head’s Y-axis was oriented along the radius of the circle, the X-axis along its circumference; hence the Z-axis was parallel to the rotation axis. The X-response of all sensors versus motor steps is depicted in Fig. 9.7b. The 1067 steps correspond to  $360^\circ$ . The relative orientation of the sensors (seen from above) is shown in Fig 9.7c.

Sensors 1–8 are oriented horizontally, 9–16 look downwards. Because the distances to any contrasted objects in space were comparatively large for sensors 1–8 they respond predominantly to rotation (their response shows about the same constant slope), whereas sensors 9–16 respond to a combination of  $\omega$  and  $T$ . Sensors 14/15 look to the ground near the centre of the circle and hence see hardly any motion whereas sensors 10/11 look to a point on the ground which is farthest away from the rotation centre and hence show the steepest slope in their response



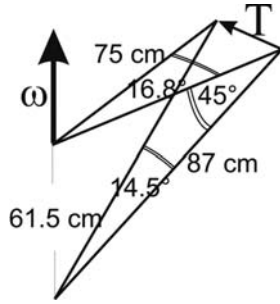


**Fig. 9.8** For the downwards looking sensor  $i$  the distance  $d^i$  to ground is about  $\sqrt{2} \cdot 61.5 \text{ cm} = 87 \text{ cm}$ . Hence  $\|T\|/d^i = \tan\{(75/87)16.8^\circ\} = \tan 14.5^\circ$ . The average fast estimate of  $1/d^i$  over all 38 subsets was  $1.7187 \pm 0.1475$ . Hence the expected value for  $T_x$  is  $T_x = \tan 14.5^\circ / 1.7187 = \tan 8.44^\circ$

was applied to each of the 38 subsets mentioned above with the fast estimate as a starting solution. The average solution of the LMI together with that of ‘fast estimates’ and the average  $E$  are shown in Table 9.2

### 9.5.2.3 Test for Evaluations of the Relative Nearness

Finally we wanted to find out if we can extract something about the 3D structure of the environment, the ‘relative nearness’ to objects within the field of view of our sensors. In an arrangement similar to the one used in the previous test the distance to ground was changed from 61 to 31 cm on a segment of  $45^\circ$  of azimuth on the circular head path (Fig. 9.10a). This was achieved by placing an elevated pattern of statistically distributed points on the ground under the circle path of head B. For each sensor fast estimates of the ‘relative nearness’ were calculated and are presented in Fig. 9.10c,d versus step number (i.e. azimuth). Note the various positions of the sensors detecting the distance change on their circle path according to the particular azimuth their line of sight crosses the distance change (for clockwise rotation, e.g. sensors 9, 16 detect the change first, 12, 13 last and for counterclockwise rotation in reverse order). The detection of  $\|T\|/d^i$  is possible but noisy.

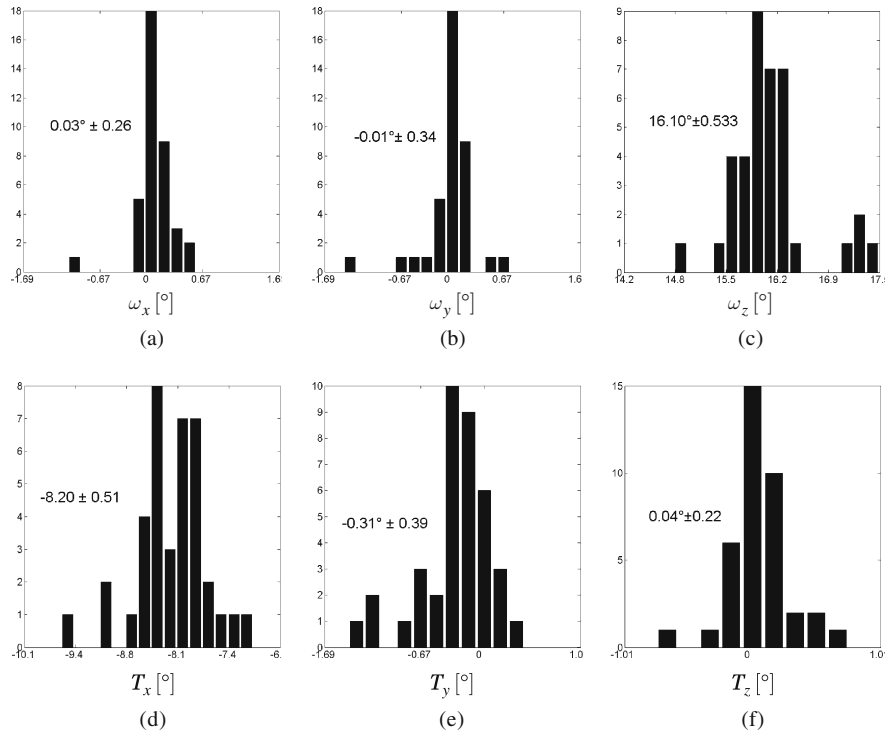
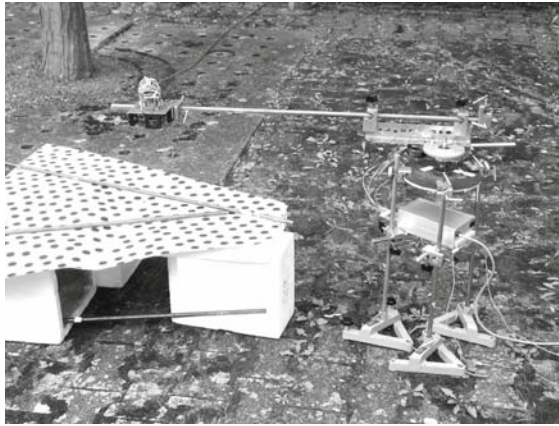


**Fig. 9.9** The distribution of  $\omega_x$  (a),  $\omega_y$  (b),  $\omega_z$  (c),  $T_x$  (d),  $T_y$  (e),  $T_z$  (f) estimated from 38 subsets of 50 subsequent motor steps along the circle path of head B (i.e. of  $16.82^\circ$  rotation angle). The

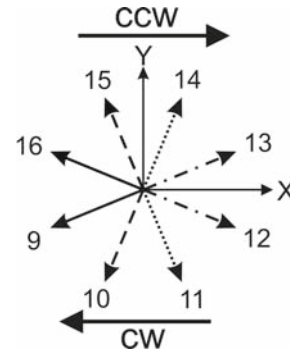
mean and standard deviation are indicated by numbers in each subplot. The expected values of  $\omega$  and  $T$  are  $\omega = (0, 0, 16.8^\circ)$  and  $T = (-8.44^\circ, 0, 0)$  (see text)

**Table 9.2** Fast  $\omega$ -,  $\mathbf{T}$ -estimates and LMI results and  $\sum_i F^2$ 

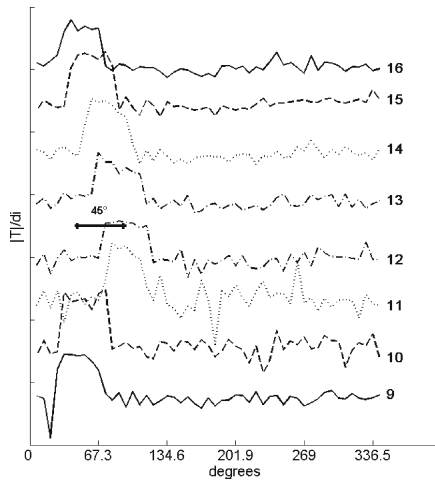
	Fast estimates			Marquardt–Levenberg iteration		
	X	Y	Z	X	Y	Z
Rotation	0.0293°	−0.01323°	16.1001°	−0.0385°	−0.1750°	18.0081°
Translation	−8.2102°	−0.3056°	0.0415°	−8.1135°	−0.2934°	−0.1792°
$E = \sum_i F^2$		28.43			7.59	



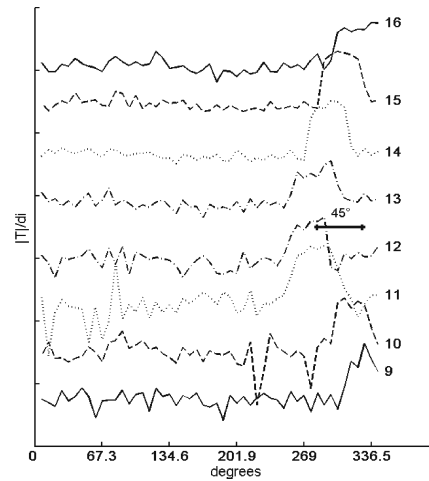
(a)



(b)



(c)



(d)

**Fig. 9.10** On an azimuth segment of  $45^\circ$  of the circular head path the distance to ground was changed from 61 to 31 cm. A pattern of statistically distributed points was placed on the ground under the circle path of head B. The pattern was elevated by 30 cm and  $45^\circ$  wide in azimuth (Fig. 9.10a) along the circular head path. The alignment of the down looking sensors (seen from above) is depicted in Fig. 9.10b. Head B was moved clockwise (in  $-X$  direction) and counterclockwise (along the  $X$  direction) in the same way as in the previous test. The result-

ing ‘relative nearnesses’  $\|\mathbf{T}\|/d^i$  are depicted in Fig. 9.10c,d for cw and ccw rotation, respectively, of the rod. Note the various angles of azimuth (i.e. step number) when the sensors detect the distance change according to their particular line of sight. The baseline for the various plots was lifted to demonstrate the individual response of each sensor. Only for the lowest trace of sensor 9 the increase of  $\|\mathbf{T}\|/d^i$  by a factor of two can be appreciated. The horizontal bar indicates  $45^\circ$

## 9.6 Discussion

For self-motion estimates the advantage of an omnidirectional motion field over the limited field of view of a normal camera has been demonstrated [2, 14, 26]. Various catadioptric systems which take  $360^\circ$  panoramic images of the environment have been proposed [4, 15, 19] as well as various methods to estimate self-motion from omnidirectional flow [14, 20, 26]. We used the algorithm proposed by Koenderink and van Doorn [18] to extract ‘best-fit’ self-motion parameters from flow seen by an omnidirectional spherical camera with a single centre of projection from all directions in space. ‘Best fit’ means that the sum of square deviations between flow measurements along various lines of sight and the theoretical flow induced in the direction of the same lines of sight by a simultaneous hypothetical rotation and translation is minimized. In a static environment with sufficient contrast (outdoor) we always find a well-defined minimum.

We used that algorithm in order to find self-motion estimates for simulated error-loaded flow fields from all possible combinations of rotation and translation, various optical systems, fields of view and environments [6, 7]. The result of these extensive simulations was that except for special cases it is best to look along pairs of opposite lines of sight and distribute these pairs over an as large as possible solid angle. Only a few of these pairs are necessary to estimate self-motion to a surprising high degree of precision. In our head B we implemented a ring of four pairs of sensors looking in opposite (preferably horizontal) directions.

The advantages of motion detectors looking into a set of fixed selected directions over a camera are obvious:

1. Motion detection by mouse chips is at least 20 times faster than by a camera. There is no need to wait for finishing a frame. Flow needs not be extracted but is determined by a fast dedicated hardware.
2. Motion detection is done in parallel along as many lines of sight as sensors are used (simultaneous distributed flow extraction).
3. The arrangement of lines of sight of the sensors and the optics can be adjusted to the intended purpose (self-motion estimate while moving over ground, flying, obstacle avoidance, etc.)

4. Sensors are light, cheap and can be attached to various locations on the vehicle.

Disadvantages are:

1. Objects cannot be discriminated.
2. Calibration may be a problem.
3. Enough sensors must see contrast along their line of sight. But sensors that do not see enough contrast or respond irregularly may be excluded from motion estimate.

We demonstrate that with our sensor heads self-rotation vectors can be estimated to a precision of  $0.5^\circ$  in each axis. The direction of self-translation can be extracted also to about  $0.5^\circ$  in each component. A rough overview of relative distances in the environment can be obtained from the ‘relative nearness’ estimates.

Because the mouse chips are light, cheap, robust, fast, easy to mount on a robot’s body and can be adapted in their optical design (distribution of optical axes and focal length of the lenses) to a desired task, it is tempting to think of their use on flying robots. For this purpose it is necessary to replace the PC, i.e. to find a sufficiently light, small and powerful microprocessor board to collect the data synchronously in parallel from all sensors and to solve the somewhat complicated task to extract the self-motion parameters from the sensor data sufficiently fast without the USB data transfer.

## References

1. Baird, E., Srinivasan, M.V., Zhang, S., Lamont, R., Cowling, A.: From Animals to Animats 9, Proceedings 9th International Conference on Simulation of Adaptive Behaviour, SAB, Rome. Visual Control of Flight Speed and Height in the Honeybee, pp. 40–51. Springer-Verlag Berlin Heidelberg (2006)
2. Baker, P., Fermüller, C., Aloimonos, Y., Pless, R.: A spherical eye from multiple cameras (makes better models of the world). Proceedings IEEE Computer Society Conference on Computer Vision and Pattern Recognition CVPR 2001, vol. 1, pp. 576–583 (2001)
3. Baker, P., Ogale, A.S., Fermüller, C., Aloimonos, Y.: The argus eye: A new tool for robotics. IEEE Robotics and Automation Magazine: Special Issue on Panoramic Robots **11** Nr. 4, 31–38 (2004)

4. Chahl, J.S., Srinivasan, M.V.: Reflective surfaces for panoramic imaging. *Applied Optics* **36**(31), 8275–8285 (1997)
5. Dahmen, H.: Eye specialisation in waterstriders : an adaptation to life in a flat world. *Journal of Comparative Physiology A* **169**, 623–632 (1991)
6. Dahmen, H., Franz, M.O., Krapp, H.G.: *Extracting Ego-motion from Optic Flow: Limits of Accuracy and Neural Matched Filters*. *Motion Vision*, pp. 143–168. Springer-Verlag Berlin Heidelberg New York (2001)
7. Dahmen, H., Wüst, R.M., Zeil, J.: Extracting egomotion parameters from optic flow: principal limits for animals and machines. *From Living Eyes to Seeing Machines*, pp. 174–198. Oxford Univ Press (1997)
8. Egelhaaf, M.: *Invertebrate Vision. The neural computation of visual motion information*, pp. 399–461. Cambr. Univ. Press (2006)
9. Egelhaaf, M., Kern, R.: Vision in flying insects. *Current Opinion in Neurobiology* **12**, 699–706 (2002)
10. Egelhaaf, M., Kern, R., Lindemann, J.P., Braun, E., Geurten, B.: *Active Vision in Blowflies : Strategies and Neuronal Mechanisms of Spatial Orientation*. Chapter 4 of this book. Springer-Verlag Berlin Heidelberg (2009)
11. Franceschini, N., Ruffier, F., Serres, J.: *Insect Pilots : Vertical and Horizontal Guidance*. Chapter 3 of this book. Springer-Verlag Berlin Heidelberg (2009)
12. Franz, M.O., Krapp, H.G.: Wide-field motion-sensitive neurons and matched filters for optic flow fields. *Biological Cybernetics* **83**, 185–197 (2000)
13. Fry, S.N.: *Experimental approaches toward a functional understanding of insect flight control*. Chapter 1 of this book. Springer-Verlag Berlin Heidelberg (2009)
14. Gluckman, J., Nayar, S.K.: Ego-motion and omnidirectional cameras. *Proceeding of the 6th International Conference on Computer vision (ICCV'03)* (2003)
15. Grassi, V., Okamoto, J.: Development of an omnidirectional vision system. *Journal of the Brazilian Society of Mechanical Science and Engineering* **XXVIII**, No. 1, 58–68 (2006)
16. Junger, W.: Waterstriders (*Gerris paludum* f) compensate for drift with a discontinuously working visual position servo. *Journal of Comparative Physiology A* **169**, 633–639 (1991)
17. Junger, W., Dahmen, H.: Response to self-motion in waterstriders: visual discrimination between rotation and translation. *Journal of Comparative Physiology A* **169**, 641–646 (1991)
18. Koenderink, J.J., van Doorn, A.J.: Facts on optic flow. *Biological Cybernetics* **56**, 247–254 (1987)
19. Nayar, S.K.: Catadioptric omnidirectional camera. *Proceedings IEEE Conference CVPR*, pp. 482–488 (1997)
20. Shakernia, O., Vidal, R., Sastry, S.: Omnidirectional ego-motion estimation from back-projection flow. *IEEE Workshop on Omnidirectional Vision* (2003)
21. Pless, R.: Using many cameras as one. *Proc. IEEE CVPR'03*, vol. 2, pp. 587–593 (2003)
22. Press, W., Flannery, B., Teukolsky, S., Vetterling, W. (eds.): *Numerical Recipes in Pascal. Nonlinear Models*, pp. 572–580. Cambridge University Press (1989)
23. Srinivasan, M., Zhang, S., Chahl, J., Barth, E., Venkatesh, S.: How honeybees make grazing landings on flat surfaces. *Biological Cybernetics* **83**(3), 171–183 (2000)
24. Srinivasan, M., Zhang, S., Lehrer, M., Collett, T.: Honeybee navigation en route to the goal: visual flight control and odometry. *Journal of Experimental Biology* **199**(Pt 1), 237–244 (1996)
25. Srinivasan, M.V., Thurrowgood, S., Soccol, D.: From visual guidance in flying insects to autonomous aerial vehicles. Chapter 2 of this book. Springer-Verlag Berlin Heidelberg (2009)
26. Vassallo, R.F., Santos-Victor, J., Schneebeil, H.J.: A general approach for egomotion estimation with omnidirectional images. *Proceedings of the Third Workshop on Omnidirectional Vision*, 97–103 (2002)
27. Zeil, J., Boeddeker, N., Stürzl, W.: *Visual Homing in Insects and Robots*. Chapter 7 of this book. Springer-Verlag Berlin Heidelberg (2009)
28. Zufferey, J.C., Beyeler, A., Floreano, D.: *Optic Flow to Steer and Avoid Collisions in 3D*. Chapter 6 of this book. Springer-Verlag Berlin Heidelberg (2009)